Broadband and High-Efficiency Manipulation of Transmitted Vortex Beams via Ultra-Thin Multi-Bit Transmission Type Coding Metasurfaces

SHAHID IQBAL[1], **MUHAMMAD RIZWAN AKRAM**[2], **(Graduate Student Member, IEEE),**
MUHAMMAD FURQAN[3], **(Graduate Student Member, IEEE), HAMZA AHMAD MADNI**[4],
MUHAMMAD ISMAIL KHAN[5,6], **AND GUOXIANG SHU**[7]

[1]State Key Laboratory of Millimeter Waves, Southeast University, Nanjing 210096, China
[2]Department of Electronic Engineering, Shanghai Jiao Tong University, Shanghai 200240, China
[3]National Mobile Communication Research Laboratory, Southeast University, Nanjing 210000, China
[4]Department of Computer Engineering, Khwaja Fareed University of Engineering and Information Technology, Rahim Yar Khan 64200, Pakistan
[5]Department of Electrical Engineering, COMSATS Institute of Information Technology, Attock Campus, Attock 43600, Pakistan
[6]Beijing Institute of Technology, Beijing 100081, China
[7]College of Electronics and Information Engineering, Shenzhen University, Shenzhen 518060, China

Corresponding author: Shahid Iqbal (shahid@seu.edu.cn)

ABSTRACT A transmission-type digital coding metasurface with features of ultrathin thickness and high efficiency over a wide operating bandwidth is proposed. The proposed metasurface is composed of low profile cascaded meta-atoms that can control the cross-polarized transmitted waves in the broad spectrum of K-band. The effectiveness of the proposed method based on the predesigned coding sequences is demonstrated by realizing various vortex beams (VB) that carry higher-order orbital angular momentum (OAM) under normal and oblique incidences. VB with flexible feature and multiple VBs from the same aperture are also realized by using the convolution operation. Two samples with 3-bit and 2-bit resolutions are fabricated to experimentally demonstrate the simulated results with single and multiple VBs. The proposed design can be easily extended to other frequency regimes to realize similar functionalities. We believe that the proposed design will find potential applications in the transmission-type optical devices.

INDEX TERMS Metamaterials, coding metasurfaces, vortex beam, orbital angular momentum, optical devices.

I. INTRODUCTION

Metasurfaces (MSs) are two-dimensional (2D) versions of metamaterials (MMs) composed of periodic or aperiodic sub wavelength resonators. These artificial structures have minimized many challenges and drawbacks presented in 3D metamaterials such as design complications, fabrication challenges, and high losses. So far, MSs have been applied to achieve numerous functionalities such as anomalous reflection / refraction [1], invisibility cloaking [1], perfect lensing [2], [3] and vortex/Bessel beam generation [4], [5]. With their flat, thin, and easy to fabricate features, MSs are attractive choice for effective control of transmitted and reflected electromagnetic (EM) waves, photonics and even in acoustic domain.

To simplify the design procedure, the concept of coding metasurface (CM) [6] is proposed, which provides more freedom of EM-wave manipulation than conventional MS. Each building block in CM is termed as a coding particle, whose phase response can be mapped on binary number N-bit ($N = 1, 2, 3, \dots$) based on the number of discrete transmission or reflection phases. In the past few years, CMs have been

The associate editor coordinating the review of this manuscript and approving it for publication was Kuang Zhang.

widely studied to realize various EM properties and to design different functional devices in microwaves, terahertz and acoustic regimes [7], [18]. Different from the aforesaid passive coding MS, the real-time control of EM waves has been achieved using active elements. In this regard, programmable MSs [9] have been realized with PIN diodes and / or varactor diodes, and real time control is achieved by time modulation. Thus, the idea of CM is not only limited to EM waves but it can also be used to design acoustic CM [10], [11]. For this purpose, an acoustic CM has been designed to split and focus the sound waves in a certain bandwidth (BW) [10]. Furthermore, a multiband asymmetric transmission device for acoustic waves has also been investigated based on the same concept [11].

The digital characteristic of CM allows us to study them from the perspective of information science. From this perspective, many digital algorithms can be performed. For example, convolution operation has been proposed to steer the reflected beam to the arbitrary direction [12]. In Ref. 16, it has been demonstrated that the amount of information carried by a CM can be evaluated by the Shannon Entropy, which exposes the relationship between the coding pattern and its radiation pattern. Furthermore, to realize multiple functionalities from the same device, bi-functional and multifunctional CM have been demonstrated. In this regard, anisotropic CM [16] and frequency dependent CM [17] were designed to realize independent functionalities based on the orthogonal polarizations and different frequency bands, respectively. Moreover, multitasking CM [18] has been realized to perform various distinct functionalities in each frequency band. Whereas, CM provides new methods to generate vortex beam (VB) that carry orbital angular momentum (OAM) with more flexibility in both transmission and reflection modes [18], [29], [30], that were challenging to be realized in traditional MS so far [19], [29].

For reflection mode, MSs have been explored a lot owing to ease in tailoring electric and magnetic response. Although, some works have been reported for transmission-type coding MSs [31], [32]. However, they suffered few issues, i.e., narrow BW, multiple cascaded layers and high angular sensitivity [33], [35]. Therefore, wide band transmissive MSs are rarely explored having high angular stability.

Here, we proposed a novel transmission-type CM with the features of high efficiency, ultrathin thickness, high angular stability and wide BW. It is worth mentioning that the BW of the proposed design is $BW = 0.098\lambda \approx 10°/°$, which is not ultra-broadband, but still broader than many previously reported designs. In this regard a comparison between the BW and some other features of the proposed and previously reported designs have been made in Table 1. Meanwhile, the wideband of the proposed design is achieved by exploiting Fabry- Perot mechanism. Although, this have been recently proposed by using continuous gratings which completely block one polarization [36]. On contrary to that concept, here, we utilized the discrete elements to block only desired band and the proposed design remains transparent for the

entire operating band. To validate the proposed concept, three different coding MSs are designed, simulated and experimentally tested for higher-order OAM generation with either 2-bit or 3-bit coding cases. In addition, the convolution operation is applied to realize the VB with steering features and also to generate multiple VBs from the same aperture. The simulation and experimental results of VBs confirms the validity of the proposed scheme.
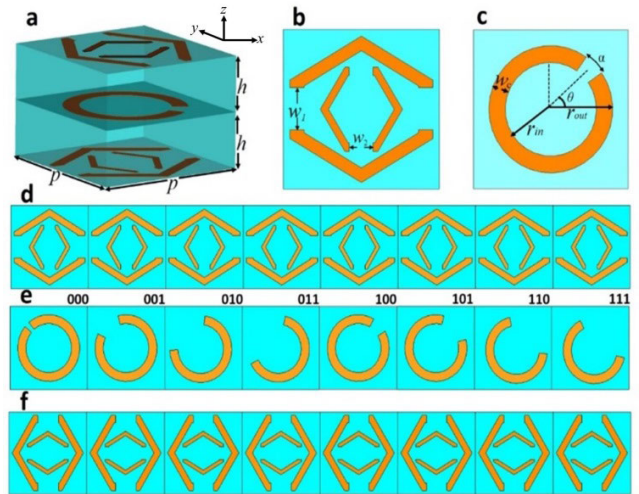

FIGURE 1. Unit cell design of 3-bit transmission type coding MS. (a) Transparent perspective view of the unit cell. (b) Top view of the unit cell and (c) Inner layer of the unit cell. (d, e, f) Top, middle and bottom layer view respectively of 3-bit coding particles (e) It can be noticed that the rotation and opening angles for the 3-bit coding MS are $\theta/\alpha = -45°/10°, -45°/55°, -45°/95°, -45°/120°, 45°/30°, 45°/40°, 45°/70°, 45°/127°$. The other geometric parameters are as follows: thickness of each substrate, $p = 6$ mm, $h = 0.6$ mm, $w_1 = 1.58$, $w_2 = 0.91$, $w_c = 0.6$ mm, radii, $r_{in} = 1.7$ mm and $r_{out} = 2.3$ mm.

II. MATERIALS AND METHODS

A. META ATOM DESIGN AND WORKING PRINCIPLE

To start with, the meta-atom in the proposed CM consist of three layers of metallic resonators, separated by two F4B dielectric substrates, as shown in Figure 1. Specially, Figure 1(a) shows a transparent view of the coding particle, Figures 1(b) and 1(c) represent the top and middle metallic layers, respectively. Similarly, Figures 1(d), 1(e) and 1(f) show the top, middle, and bottom metallic layers for all eight coding particles, respectively. All the metallic layers are made of annealed copper with a thickness 0.018mm. The dielectric spacers F4B are used with $\varepsilon = 2.65$, tangent loss $\delta = 0.001$ and a thickness $h = 0.6$mm. The overall thickness of the proposed meta-atom is 1.254mm ($\lambda/12$ at operating frequencies), that is thinner than previous cascaded coding meta-devices [30], [32]. The top and bottom layers have hexagonal double split-ring resonator (DSRR) with their openings oriented orthogonal to each other. While, the middle layer consists of C shaped split-ring resonator (CSRR) that is responsible for imparting different phase responses for the transmitted waves. Simulations of the proposed meta-atom under normally incident *y*-polarized plane waves propagating

along '-*z*' direction are carried out in CST MWS (Computer simulation technology Microwave studio) with unit cell boundary conditions.

The working principle of the meta-atom can be explained as follows: the proposed design can be treated as quasi ABA type Huygens structure [40], [42], where the top and bottom layers are oriented orthogonal to each other. It has already been demonstrated that the ABA type MS has the ability of EM wave tunneling [43] which can be explained using effective medium theory. More comprehensive explanation of this type cascaded MSs can be found in Ref. [44].
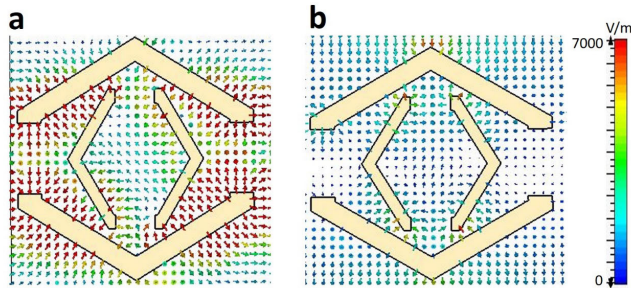

FIGURE 2. Electric field distribution at the bottom layer at central frequency. (a) Electric field distribution under *y*-polarized incidence. (b) Electric field distribution under *x*-polarized incidence.

Furthermore, the current analysis of the proposed design is shown in Figure 2. It can be seen from Figure 2(a), that an electric dipole is induced along *y*-direction in the bottom layer. This dipole completely blocks the *x*-polarized wave for the desired band and acts transparent for *y*-polarized incident as obvious from Figure 2(b). The asymmetrically placed CSRR acts as polarization converter as a result of excited electric dipoles along 45° to the incident wave. The *y*-polarized wave is fully converted to *x*-polarization and transmits to the other side as a result of multiple polarization conversions by CSRR and reflections by the top and bottom orthogonally induced dipoles. Moreover, the broadband operation from the proposed design is achieved by exploiting Fabry-Perot cavity mechanism [36].

For further explanation, a comparison of the performance of coding particle is presented in Figure 3, where Figures 3(a) and 3(b) show the current densities for both without and with small hexagonal resonator, respectively. It can be observed that by adding an orthogonally oriented smaller hexagonal DSRR on both top and bottom layers of the meta-atom, the induced current strengths increase, which causes the near field coupling stronger. Thus, the cross-polarized transmission amplitude can be increased as compared to the meta-atom, which contains only larger hexagonal DSRR. Moreover, the transmission amplitude of coding particle without small hexagonal DSRR can be seen in Figure 3(c), whereas, Figure 3(d) gives the transmission amplitude of coding particle with small hexagonal DSRR. Further, we also simulated the unit cell in which the smaller and larger hexagonal DSRR has the openings in the same direction. In doing this, we observed that although the phase
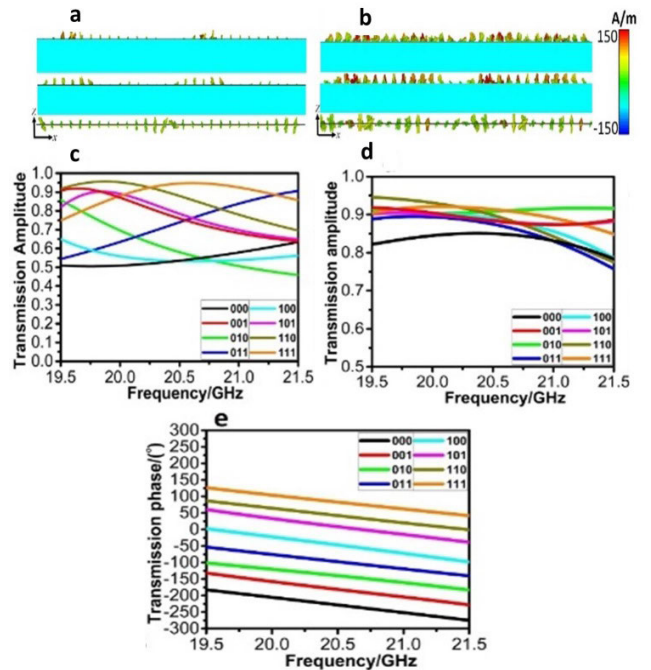

FIGURE 3. Comparison of the performances of meta-atom with and without small hexagonal resonator and the corresponding phase and amplitude responses. (a) Current distribution on each layer of unit cell without a small hexagonal resonator. (b) Current distribution on each layer with small hexagonal resonators. (c) Amplitude response of 3-bit unit cells without a smaller hexagonal resonator. (d) Amplitude response of 3-bit unit cells with a smaller hexagonal resonator. (e) 3-bit transmission phase response. Note: For a clear view of the current distribution we took separate picture of each layer in the unit cell and then combine it.

(not shown in figures for brevity) remains the same but the amplitude falls to almost 50% of the results of the proposed design (Figure 3(d)). Thus, it can be concluded that the optimal results from the proposed meta-atom can be obtained with only the orientations of the metallic resonators like that of Figure 1.

The gap of SRR in the middle layer is oriented at $\theta = 45°$ or $\theta = 135°$ and is asymmetric with respect to *x*-axis and *y*-axis. The incident electric field excites resonances at the ends of the SRR that converts the polarization of the incident waves. The function of the proposed SRR is exactly similar to complementary SRR, as presented in Ref. [38], [45], which interacts with the incoming EM field leading to current transfer resulting in electric field perpendicular to the original one.

Moreover, Jones matrices [46] can also be used to study the functionality of the proposed meta-atom. In the proposed design a plane wave with time harmonic dependency $e^{i\omega t}$ and propagating in the forward "-z" direction impinges on the top surface of meta-atom which can be written mathematically as:

$$E_i(r, t) = \begin{bmatrix} i_x \\ i_y \end{bmatrix} e^{-i(kz-\omega t)} \qquad (1)$$

where 'ω' is the frequency and $k = \frac{2\pi}{\lambda}$ is the wave vector, while the entries i_x and i_y in the matrix describes the

polarization states of the incident wave. Similarly, the transmitted field can be mathematically described as:

$$E_t(r, t) = \begin{bmatrix} t_x \\ t_y \end{bmatrix} e^{-i(kz-\omega t)} \qquad (2)$$

Similarly, the transmission matrix which generally connects the complex amplitudes of the incident and transmitted waves can be written as:

$$\begin{bmatrix} t_x \\ t_y \end{bmatrix} = \begin{bmatrix} T_{xx} & T_{xy} \\ T_{yx} & T_{yy} \end{bmatrix} \begin{bmatrix} i_x \\ i_y \end{bmatrix} = \begin{bmatrix} A & B \\ C & D \end{bmatrix} \begin{bmatrix} i_x \\ i_y \end{bmatrix} = T \begin{bmatrix} i_x \\ i_y \end{bmatrix} \qquad (3)$$

Here in the above equation for simplicity the entries $T_{i,j}$ are replaced with A, B, C and D. Now the 'T' matrix for a simple anisotropic structure with a mirror plane parallel to y-axis can be written as:

$$T = \begin{bmatrix} A & 0 \\ 0 & D \end{bmatrix}$$

Meanwhile, rotation by an angle Φ will result the matrix as

$$D_\varphi = \begin{bmatrix} \cos(\varphi) & \sin(\varphi) \\ -\sin(\varphi) & \cos(\varphi) \end{bmatrix} \qquad (4)$$

which will modify the transmission matrix from T to $T_\varphi = D_\varphi^{-1} T D_\varphi$.

The anisotropic split ring resonator is sandwiched by two hexagonal double split ring resonator pairs, where its T matrix can be described as:

$$T_{hex}^\perp = \begin{bmatrix} 1 & 0 \\ 0 & 0 \end{bmatrix} \text{ and } T_{hex}^\parallel = \begin{bmatrix} 0 & 0 \\ 0 & 1 \end{bmatrix} \text{ that modify the final}$$

transmission matrix from T to $T_{new} = T_{hex}^\perp T_\varphi T_{hex}^\parallel$.

In special circumstances when the orientation angle $\theta = 45°$ or $\theta = 135°$, two transmission matrices are obtained, which have equal magnitude but opposite phases, that can be mathematically written as:

$$T_{45°} = \begin{bmatrix} 0 & A-D \\ 0 & 0 \end{bmatrix}, \quad T_{135°} = \begin{bmatrix} 0 & -(A-D) \\ 0 & 0 \end{bmatrix}$$

The two transmission matrices reveal that the CSRR oriented with 45° and 135° have the same cross polarized transmission amplitudes but with an 180° phase difference. It also predicts the fact that a phase coverage of only 180° is required to control for the whole 360° phase at one orientation, as the other 180° phase can be realized by just rotating the CSRR from $\theta = 45°$ to $\theta = 135°$.

Moreover, the wide band and high efficiency transmittance is realized by the virtue of a Fabry Perot like cavity phenomenon occurring in the proposed structure. When a y-polarized plane wave interacts with the meta-atom, the top hexagonal pair allows it to enter, which then interacts with CSRR and converts to x-polarized states. After this conversion the x-polarized part transmitted can go onward while the reflected part interacts with top layer, which again reflect it inside the meta-atom. In this way the reflected wave which now has again y-polarization interacts with SRR and converts to x-polarized state that enhances the operation in a wide frequency range.

To obtain the desired transmitted phase response that can be mapped on binary numbers 000, 001, 010 and so on, we used a C-shaped split ring resonator (CSRR) in the middle layer with different orientations and openings as shown in Figures 1(c) and 1(e). Meanwhile, Figure 1(e) shows all the orientation and opening angles of the 3-bit coding particles. It is worth mentioning that, CSRR is excited in response to the incident linearly polarized waves, generating electric response at the operating frequencies which couples with Fabry-Perot resonances to give wide band response, as explained in antenna array theory [34]. At the designed frequency, the circumference of the arc is nearly equal to the half wavelength, i.e., $\lambda/2 = 2\pi X - X\alpha$, where $X = \frac{(R_{out}+R_{in})}{2}$.

In the proposed 3-bit CM, initially, we keep the orientation of CSRR at $\theta = -45° = 135°$ and optimize the opening angle 'α' to obtain the desired four transmission phases corresponding to coding states, 000, 001, 010 and 011, respectively. The corresponding values of the parameters 'θ/α' for the above-mentioned phases are: - 45°/10°, - 45°/55°, - 45°/95°, -45°/120°. Similarly, to obtain the other four desired phase responses, we apply the fact, that by rotating the SRR with angle 'θ' will modify the transmission phase to $\Phi° \pm 2\theta$, where '$\Phi°$' is the transmission phase for '000' digital state when the orientation of SRR is: $\theta = 45°$. In this manner, we rotate the CSRR to $\theta = -\theta$, i.e. ($\theta = 45°$) and optimize the opening angle 'α' to obtain the remaining four desired transmission phase responses, i.e., 100, 101,110 and 111, where the corresponding optimized values of 'θ/α' are: 45°/30°, 45°/40°, 45°/70°, 45°/127°. The corresponding amplitude responses are presented in Figure 3(d), which almost have same (constant) values i.e. '$A^T \geq 0.82$', which for most of the coding states reaches to 0.90 except the '000' coding states. It should be noted that, this small amplitude difference of 0.90-0.82 puts no significant difference in the results of the full structure.

Besides, phase differences between adjacent coding states are about $45° \pm 7°$ at the center frequency of *20.5 GHz*, shown in Figure 3(e). In addition, the design has the property to operate for the normally incident waves propagating along '$+z$' direction but with orthogonal polarization in the same working band.

III. RESULTS AND DISCUSSIONS

CM gives us the freedom to achieve different functionalities by changing spatial distribution of coding meta-atoms. Our proposed design operating in broadband regime can completely control the transmitted wave (cross polarized) due to the availability of eight meta-atoms with almost equally distant smooth phases and almost constant high transmission amplitudes of the cross-polarized field. Various full structures for different functionalities are designed and in each case the concept of the super unit cell is applied to avoid unnecessary interference and to have freedom of designing full structures with different periods of the coding sequences, so as to manipulate the transmitted waves with more flexibility. In the following, full-wave simulations are carried out by using CST

MWS under both normally and obliquely incident *y*-polarized plane waves propagating along '-*z*' direction to record both near and far-field patterns.

A. HIGHER ORDER VBs GENERATION

VBs find its applications in modern communication systems and other optical manipulations [35], [37]. The azimuthal phase dependence of the VB can be expressed as $\exp(il\varphi)$, where the phase distribution is described by the following equation.

$$\phi(x, y) = l \times \tan^{-1}(y/x) \tag{5}$$

In Equation (5) x, y are the spatial coordinates and ''l'' is the topological charge of OAM carried by vortex beam.
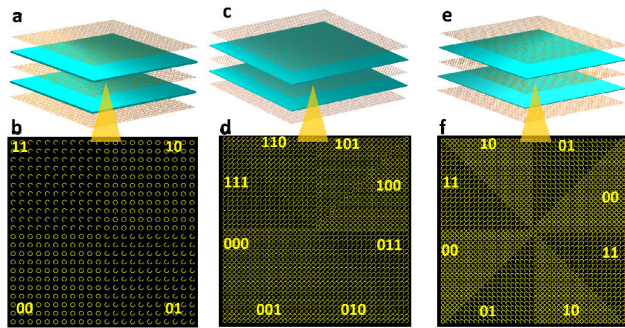

FIGURE 4. Hardware architectures of vortex beam generators, (a,b) Staged view of full structure for CV1 and the corresponding middle layer. (c, d) Staged view of full structure for CV2 and the corresponding middle layer. (e, f) Staged view of full structure for CV3 and the corresponding middle layer.

In the proposed 3-bit CM, we have the freedom to design VB generators by using either four coding particles hardware (which mimic the 2-bit coding case) or all eight particles hardware (which mimic 3-bit coding case), as shown in Figure 4, where Figures, 4(a), 4(c) and 4(e) show the full structures hardware architectures of CV1 (coding VB generator with '$l = 1$'), CV2 and CV3, while Figures, 4(b), 4(d), and 4(f) show their corresponding middle layers, which show the phase distribution.

Firstly, we design a VB generator labelled 'CV1' composed of 2-bit meta-atoms only. The design 'CV1' is made by dividing the area into four equal sections and each of these sections is encoded with only one coding particle of the 2-bit meta-atoms, so as to introduce a 2π phase loop of the 2-bit meta-atoms, to introduce a 2π phase loop (see Figure 5(a)). In Figure 5(b), the near field intensity has a donut like shape in the cutting *x-y* plane, which is observed 180 mm away from the surface. Similarly, Figures 5(c) and 5(d) show the absolute and real part of near field intensity in the cutting *x-z* plane, respectively, where a null at the centre and non-diffractive nature, the two characteristics of a vortex beam are obvious. The phase pattern which should have one period in the 2π radians for '$l = 1$', is shown in Figure 5(e), in the *x-y* cutting plane. Moreover, Figures 6(a) and 6(b) show

the far-field pattern in 3D and 2D planes of the generated VB, which clearly shows that a VB is generated with high efficiency as the difference between the null and maximum annular intensity is almost *20 dB*.
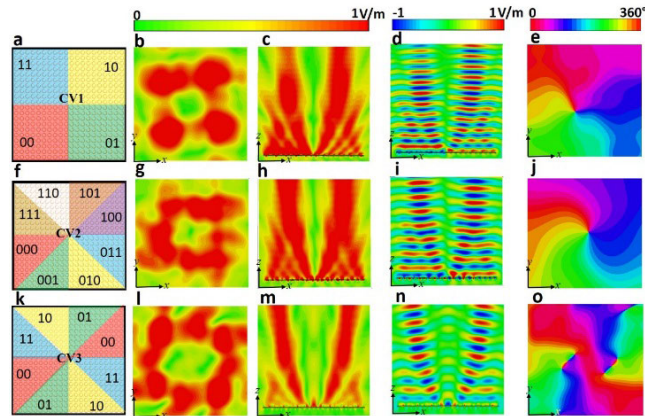

FIGURE 5. Near field intensities and phase patterns of vortex beam carrying OAM of order '$l = 1$' and '$l = 2$'. (a) 2-bit coding MS 'CV1' for vortex beam generation with $l = 1$. (b, c) Near field intensities in the *x-y* and *x-z* cutting plane with $l = 1$. (d) Real part of near field intensity (Electric field) in the *x-z* cutting plane with $l = 1$ (e) Phase response of OAM with $l = 1$ in the *x-y* cutting plane. (f) 3-bit coding MS 'CV2' for vortex beam generation with $l = 1$. (g, h) Near field intensities in the *x-y* and *x-z* cutting plane with $l = 1$. (i) Real part of near field intensity in the *x-z* cutting plane with $l = 1$ (j) Phase response of OAM with l = 1 in the *x-y* cutting plane. (k) 2-bit coding MS 'CV3' for vortex beam generation with $l = 2$. (l, m) Near field intensities in the *x-y* and *x-z* cutting plane with $l = 2$. (n) Real part of near field intensity (Electric field) in the *x-z* cutting plane with $l = 2$ (o) Phase response of OAM with $l = 2$ in the *x-y* cutting plane.

In the second phase, we employ all the available eight coding particles to design a VB generator labelled 'CV2' which also can carry OAM of order '$l = 1$' but with different hollow width and intensity. For this purpose, the design 'CV2' is equally divided into eight sections and each section is encoded with one meta-atom among the 3-bit coding particles, as shown in Figure 5(f). Moreover, the same procedure as in 'CV1' is adopted to simulate the design 'CV2'. Interestingly, the simulation results shown in Figures 5(g-j) and Figures 6(c-d) demonstrate that a VB has higher efficiency and smoother nature than 'CV1', indicating that efficiency can be improved by increasing the number of digital states.

To generate a higher order vortex beam that can carry OAM with $l = \pm 2$, we need to introduce a 4π phase loop. A coding VB generator labelled 'CV3' is designed by choosing 2-bit coding particles from the available 3-bit meta-atoms. The corresponding design is divided into eight equal sections where each section is filled with a coding particle among the selected 2-bit meta-atoms in such a manner to introduce 4π phase loop, as displayed in Figure 5(k). The similar scheme as in 'CV1' and 'CV2' is applied here to simulate 'CV3' under the normal incidence of *y*-polarized plane waves. Simulation result in Figure 5(l) shows the near field intensity in the *x-y* cutting plane observed at 180 mm distance from the MS plate, which has a donut like pattern with a wider hollow width as compared to 'CV1' and 'CV2'. It should be noticed that
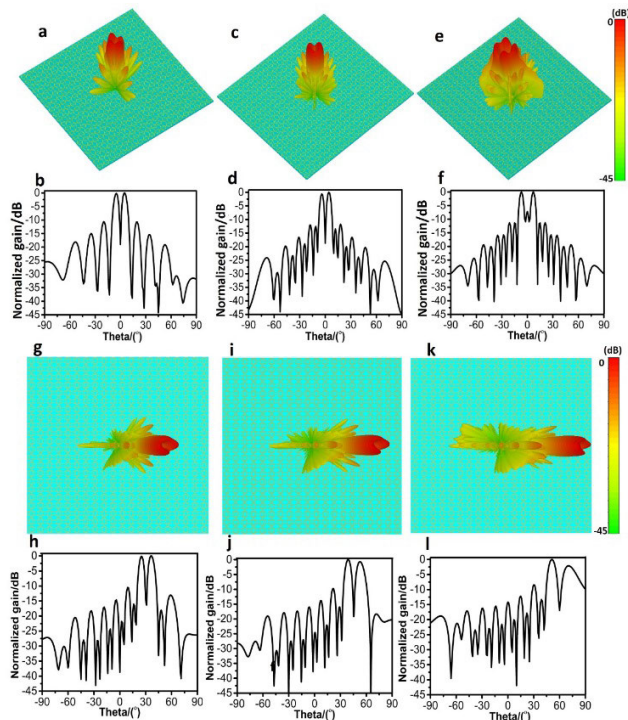
FIGURE 6. 3-D and 2-D Radiation patterns of the generated vortex beams with '*l* = 1' and '*l* = 2'. (a, b) 3-D and 2-D radiation pattern of vortex beam with *l* = 1 for 2-bit vortex beam generator 'CV2'. (c, d) 3-D and 2-D radiation pattern of vortex beam with *l* = 1 for 3-bit structure 'CV2'. (e, f) 3-D and 2-D radiation pattern of vortex beam of OAM, *l* = 2 for 2-bit structure 'CV3'. (g-l) Vortex beams generation for obliquely incident waves with different incident angles by 3-bit coding vortex beam generator 'CV2'. (g, h) 3-D and 2-D radiation pattern of the vortex beam when the incident angle is 30°. (I, j) 3-D and 2-D radiation pattern of the vortex beam when the incident angle is 45°. (k, l) 3-D and 2-D radiation pattern of the vortex beam when the incident angle is 60°.

increasing the value of '*l*' will increase the hollow width, which is due to the self-cancelling effect induced by the spiral phase distributions. Similarly, Figures 5(m-n) show the near field intensity and real part of electric field intensity in the *x-z* cutting plane respectively, which has a smooth and non-diffractive pattern. Further, Figure 5(o) shows the phase pattern of the near field in the *x-y* cutting plane where the repetition of each color confirming that the OAM has an order *l* = 2. Moreover, Figures 6(e-f) show 3D and 2D far-field patterns, respectively. The generated VB on the transmission side has a wider hollow width, but relatively lower intensity as compared to 'CV1' and 'CV2' due to the fact that for a fixed number of digital states in a MS, and increasing the topological charge '*l*' of OAM will cause a decrease in the intensity.

The other important feature of the proposed design is its ability to work for a wide range of incident angles. To demonstrate this property of the proposed design, VBs for different incident angles are investigated. For this purpose, we simulate the design 'CV2' illuminated by plane waves at different obliquely incident angles. The simulated results in Figures 6(g), 6(i), and 6(k) show the 3-D far-field patterns of vortex beams generated for obliquely incident

plane waves with incident angles at 30°, 45° and 60°, respectively. Similarly, Figures 6(h), 6(j), and 6(l) show the 2-D equivalents of Figures 6(g), 6(i), and 6(k), respectively. It can be noticed that the highly efficient VBs can still be generated for obliquely incident plane waves with incident angles ranging from 0° to 60°.

B. FLEXIBLE AND MULTIPLE OAM-VB GENERATION

As mentioned above, an important feature of the CM is the convolution operation which leads to the realization of scattered (reflected or transmitted) beams to arbitrary directions. The convolution operation in CM has been discussed in detail in Ref. 13, where it has been explained that the multiplication of two coding patterns is equal to the convolution of their corresponding scattering patterns. In this way steering a beam to arbitrary direction can be achieved by just multiplying two different coding patterns.

Interestingly, the multiplication of two different coding patterns (multiplication of phases) is equal to the binary addition of their coding digits, which means that beam steering and/or beam shaping of an arbitrary scattered beam can be obtained by adding the gradient coding sequence and/or the beam shaping coding sequence with the coding sequence of arbitrary scattered beam.

In this section, we will use the convolution operation to realize flexible and multiple VBs with high efficiency in transmission mode. For this purpose, we first add the VB coding pattern (CV1) (Figure 7(a)) to the 2-bit gradient coding sequence (Figure 7(b)) to construct a new coding pattern (see Figure 7(c)), which can provide a VB with a deflection angle 'θ_d'. The angle of deflection of VB can be calculated the same way as the angle of deflection of a scattered beam from a gradient coding MS, i.e.,

$$\theta_d = \sin^{-1}(\lambda / \Gamma) \quad (6)$$

where '$\tilde{A}$' is the period of the gradient coding sequence. The simulated results of this CM can be seen in Figure 6(d), which present a VB with a deflection angle 'θ_d' which can be further steered by just varying the period of the gradient coding sequence. In the second stage, VB coding pattern (CV1) in Figure 7(e), is added to the coding pattern in Figure 7(f), which can split the transmitted field into two equal beams with deflection angles "$\pm\theta_d$". The generated coding pattern can be seen in Figure 7(g), which has the ability to provide two VBs from the same aperture deflected at equal and opposite angles. The simulated results for this scenario are shown in Figure 7(h).

In the last case, the coding pattern of OAM-VB (Figure 7(i)) is added to the coding pattern of quad-beam generator Figure 7(j), (chess board configuration). As in the chess board configuration MS, the transmitted field shape into the quad-beam, consequently, the new coding pattern (see, Figure 7(k)), which is the addition of chess board and 'CV1' patterns provides a quad VB. The simulated results for this case can be observed in Figure 7(l). In all the three cases,
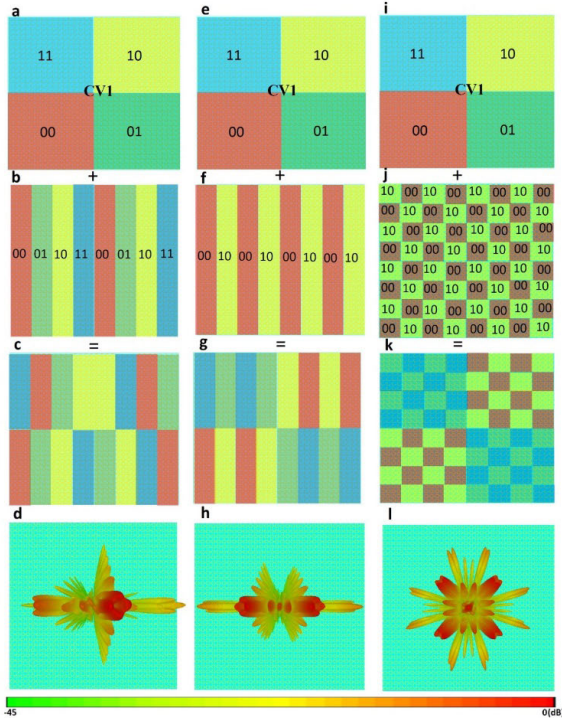
FIGURE 7. Convolution operation to realize steerable and multiple vortex beams for multiple OAM. (a, e, i) Vortex beam generator (CV1) with mode '*l* = 1'. (b) gradient coding sequence (c) coding pattern for vortex beam steering. (d) 3-D far-field radiation pattern of deflected vortex beam. (f) Coding sequence for beam splitting. (g) Coding pattern of vortex beam splitting. (h) 3-D far-field radiation pattern of split OAM vortex beam. (j) coding sequence for quad beam. (k) coding pattern of quad vortex beam. (l) 3-D far-field pattern for quad vortex beam.

the simulation results have an excellent agreement with the theoretically predicted results.

Further, since we claimed that our devices are highly efficient, thus a quantitative estimation of the efficiency is necessary. For this purpose, we calculate the working efficiency [35], [38] of the proposed designs employing the formula as:

$$\eta_t = \frac{\iint\limits_s (E_t \times H_t^*).ds}{\iint\limits_s (E_i \times H_i^*) \cdot ds} \times 100 \qquad (7)$$

which results in $\eta_t \approx 83\%$.

Further, the power reflected and absorbed can be calculated using (4) and (5), respectively.

$$P_r = \iint\limits_s (E_r \times H_r^*) \cdot ds \qquad (8)$$

$$P_a = P_i - P_r - P_t = \iint\limits_s (E_i \times H_i^*) \cdot ds$$
$$- \iint\limits_s (E_t \times H_t^*) \cdot ds - \iint\limits_s (E_r \times H_r^*) \cdot ds \qquad (9)$$

where P_i and P_t shows the incidence and transmitted power, P_r and P_a shows the reflected and absorbed powers while, E_i, E_t and E_r shows the incidence, transmitted and reflected

electric fields, respectively. Similarly, the corresponding magnetic fields are shown by H_i, H_t and H_r, respectively. It is important to mention that the evaluated efficiency, i.e. '$\eta_t \approx 83\%$' is for design 'CV2' and for normal incidence only. For oblique incidences and for design CV3, the efficiency degrades slightly but it still has the numerical values $\eta \geq 77\%$ which is still acceptable.
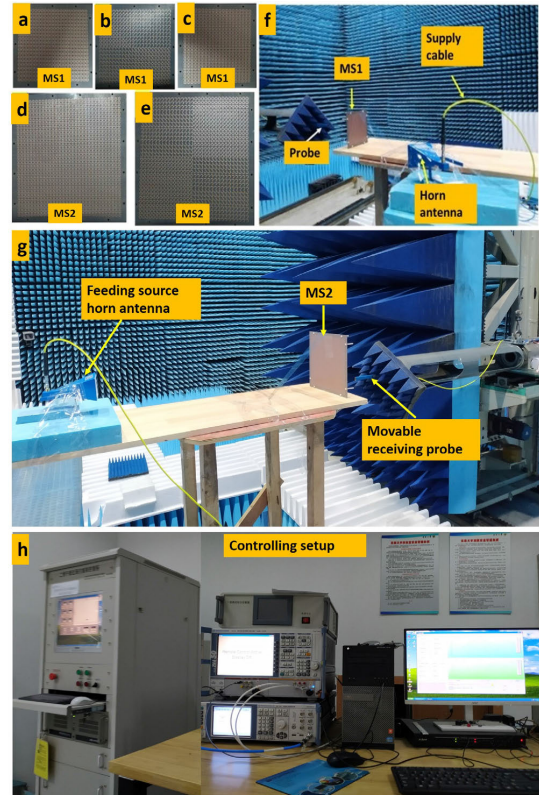

FIGURE 8. Fabricated samples and near-field experimental setup. (a, b, c) Top, middle and bottom layer of the fabricated 3-bit coding MS 'MS1' for VB generation. (d, e) Top and middle layer of the fabricated coding MS 'MS2' for split VBs. (f) Experimental set up for measuring VB under oblique illumination of *y*-polarized plane waves. (g) Experimental set up for measuring VB under normal illumination of plane waves. (h) Experimental set up for measuring split VBs under normal illumination of *y*-polarized plane waves.

IV. FABRICATION AND MEASUREMENT

In order to validate the above-simulated results, two MS samples are fabricated by using the standard PCB (printed circuit board) technology. The sample labelled as 'MS1', (see, Figure 7) has an overall size of 144×144 mm^2, which contains 22×22 unit cells. Three metallic layers, i.e., bottom, middle and top layer are displayed in Figures 8(a)- 8(c) respectively. The final structure can be seen in Figures 8(f) and 9(a), labeled as 'MS1', which is made by cascading the three layers with the help of plastic screws. It is worth mentioning that the fabricated sample 'MS1' has a 3-bit resolution with coding pattern same as that of 'CV2' to generate a VB carrying OAM with order '*l* =1'.

Similarly, another sample labelled as 'MS2' is fabricated with the coding pattern as that of shown in Figure 7(g) for split VBs where the top and middle layers of 'MS2' are
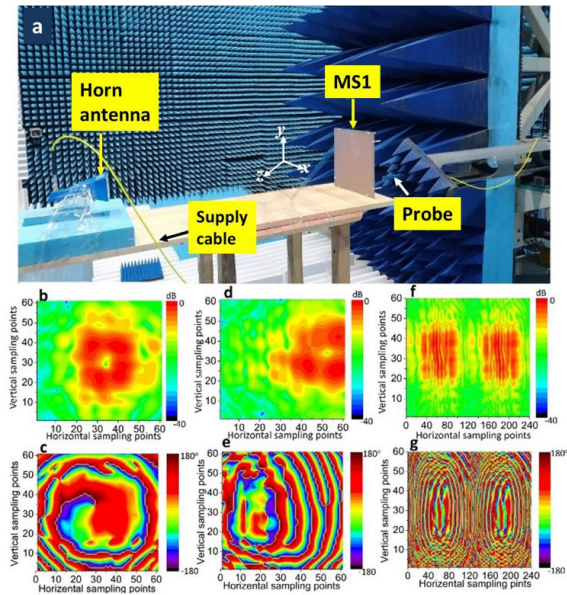
FIGURE 9. Measured near-field intensities and phase patterns for samples 'MS1' and 'MS2'. (a) Experimental setup of near field measurement for sample 'MS1' (b, c) The near-field intensity and phase pattern respectively of the VB carrying OAM with '*l* = 1' generated by 'MS1' under the normal illumination of *y*-polarized plane waves. (d, e) The near-field intensity and phase pattern respectively of the VB carrying OAM with '*l* = 1' generated by 'MS1' under the oblique illumination of plane waves. (f, g) The near-field intensities and phase patterns, respectively, of the split VB carrying OAM with '*l* = 1' generated by 'MS2' under the normal illumination of *y*-polarized plane waves.

TABLE 1. Comparison of some features of the proposed work with previous designs.

Transmission-type MS for VB generation	POLARIZATION	Working-Band and Bandwidth	Overall thickness	Angular stability In θ°	Number of VB demonstrated
Ref [31]	LP	K- band 14-16 GHz	0.2λ	N/A	single
Ref [36]	CP	X band 8-12 GHZ	0.05λ	60°	Single
Ref [47]	LP	K- band 22.4-23.8GHz	0.3125 λ	60°	single
Ref [48]	LP	X band 8-12 GHZ	0.1538 λ	N/A	single
Ref [49]	CP	X-BAND 10.1-10.9 GHz	0.1394 λ	N/A	Single
Ref [50]	LP/CP	X-BAND 9.1-10.3 GHz	0.1λ	N/A	Single
This work	LP	K-band 19.5-21.5GHz	0.083λ	60°	Multiple

shown in Figures 8(d) and 8(e), respectively. It should be noted that as the bottom layer of the 'MS2' is the same as that of the top layer, but only orthogonally oriented, which is not shown in figures for brevity here. The overall size of 'MS2' is 200×200 mm² which contains 32×32 unit cells.

For experiment, near-field microwave anechoic chamber is employed and the experimental setup is illustrated in Figures 9(a) and Figure 8(f). A rectangular horn antenna operating from 18 to 24 GHz serves as a feeding source, while the movable probe operating in the same frequency band is used to receive the cross-polarized transmitted field. In the first stage, the antenna is adjusted to impinge the *y*-polarized incident waves on sample 'MS1', meanwhile, the movable probe is adjusted 180 mm away from the sample, to scan an area of 305×305mm² with 61×61 sampling points, where the space between each two consecutive sampling points was 5mm. The measured results plotted in Figures 9(b) and 9(c) show the electric field intensity (E_x) and phase pattern respectively, and experimentally demonstrated that an efficient VB is generated carrying OAM of order '*l* = 1'.

In the second stage, we adjusted the horn antenna to impinge the incident waves obliquely (see Figure 8(f)) in order to verify the angular stability of the fabricated sample 'MS1'. The corresponding measured field intensity and phase pattern for a 45° incidence are plotted in Figures 9(d) and 9(e), respectively. It can be observed that the intensity still has a donut like shape deflected rightwards

which confirms that the design can work in a wide range of incident angles. However, due to the limitation of the area scanned by the receiving probe, we were not able to collect all the information of the realized VB, and thus a small loss in information appears in the measured results for oblique incidence case, which can be observed in Figures 9(d) and 9(e).

Further, in order to verify the generation of split VBs, we test the fabricated sample 'MS2' in the same microwave anechoic chamber, (see Figure 8(g)) by making only minor adjustments in the setup. Similar procedure as that for MS1 is employed to measure the near fields of 'MS2'. The probe in this case is adjusted to scan an area of ($x \times y = 480 \times 300$ mm²) with sampling points 240 ×60 along the horizontal and vertical axis respectively. Note that, here, the space between the two consecutive sampling points along the horizontal axis is 2mm while that of between two vertical sampling points was fixed to be 5mm. All the measured results have a close agreement with their theoretical counterparts. However, a distortion occurred in the measured results of split VBs, especially in field intensities which is due to the lower bit we have used only 2-bit (four coding particles) among the available eight meta-atoms to fabricate the sample. The other possible reasons may be the external noise and the distribution of transmitted energy due to multiple beams from the same aperture.

Moreover, the hollow in the near-field intensities in this case are very small, which is due to scanning a large area, plotting the results in the same plane and shrinking the picture. Further, it is important to verify the claimed functionalities and novelty of the proposed design. For this purpose, we compared the demonstrated design and its features (see Table. 1) with the previously reported designs.

V. CONCLUSION

We have presented a novel 3-bit transmission type CM. The proposed design has the features of ultrathin thickness, high efficiency, and broadband performance with angular stability. Various functionalities were realized by using different coding sequences with a unique distribution of coding particles. VBs were generated for both normal and oblique incident plane waves with different topological charges and distinct hollow widths by distributing the coding particles in a spiral profile. Further, flexible and multiple VBs were also realized by applying the convolution operation. Experiments for normal and oblique incidences with single and split VBs were performed by fabricating and testing two different samples, where the measured results had excellent agreement with their theoretical counterparts. We remark that the same structure can be extended to other frequency regimes to realize similar functionalities, and we believe that the proposed CM will find potential application to transmission-type optical devices.

REFERENCES

[1] N. Yu, P. Genevet, M. A. Kats, F. Aieta, J.-P. Tetienne, F. Capasso, and Z. Gaburro, "Light propagation with phase discontinuities: Generalized laws of reflection and refraction," *Science*, vol. 334, no. 6054, pp. 333–337, Oct. 2011.

[2] D. Schurig, J. J. Mock, B. J. Justice, S. A. Cummer, J. B. Pendry, A. F. Starr, and D. R. Smith, "Metamaterial electromagnetic cloak at microwave frequencies," *Science*, vol. 314, no. 5801, pp. 977–980, Nov. 2006.

[3] S. Maslovski and S. Tretyakov, "Perfect lensing with phase-conjugating surfaces: Toward practical realization," *New J. Phys.*, vol. 14, no. 3, Mar. 2012, Art. no. 035007.

[4] N. Fang, "Sub-diffraction-limited optical imaging with a silver superlens," *Science*, vol. 308, no. 5721, pp. 534–537, Apr. 2005.

[5] H. Zhang, X. Zhang, Q. Xu, Q. Wang, Y. Xu, M. Wei, Y. Li, J. Gu, Z. Tian, C. Ouyang, and X. Zhang, "Polarization-independent all-silicon dielectric metasurfaces in the terahertz regime," *Photon. Res*, vol. 6, no. 1, pp. 24–29, 2018.

[6] C. Pfeiffer and A. Grbic, "Controlling vector bessel beams with metasurfaces," *Phys. Rev. A, Gen. Phys.*, vol. 2, no. 4, Oct. 2014, Art. no. 044012.

[7] T. J. Cui, M. Q. Qi, X. Wan, J. Zhao, and Q. Cheng, "Coding metamaterials, digital metamaterials and programmable metamaterials," *Light, Sci. Appl.*, vol. 3, no. 10, p. e218, Oct. 2014.

[8] L. H. Gao, Q. Cheng, J. Yang, S. J. Ma, J. Zhao, S. Liu, H. B. Chen, Q. He, W. X. Jiang, H. F. Ma, and Q. Y. Wen, "Broadband diffusion of terahertz waves by multi-bit coding metasurfaces," *Light-Sci. Appl.*, vol. 4, no. 9, p. e324, 2015.

[9] L. Liang, M. Qi, J. Yang, X. Shen, J. Zhai, W. Xu, B. Jin, W. Liu, Y. Feng, C. Zhang, H. Lu, H.-T. Chen, L. Kang, W. Xu, J. Chen, T. J. Cui, P. Wu, and S. Liu, "Anomalous terahertz reflection and scattering by flexible and conformal coding metamaterials," *Adv. Opt. Mater.*, vol. 3, no. 10, p. 1311, Oct. 2015.

[10] X. Wan, M. Q. Qi, T. Y. Chen, and T. J. Cui, "Field-programmable beam reconfiguring based on digitally-controlled coding metasurface," *Sci. Rep.*, vol. 6, no. 1, Aug. 2016.

[11] B. Xie, K. Tang, H. Cheng, Z. Liu, S. Chen, and J. Tian, "Coding acoustic metasurfaces," *Adv. Mater.*, vol. 29, no. 6, 2017, Art. no. 1603507.

[12] B. Xie, H. Cheng, K. Tang, Z. Liu, S. Chen, and J. Tian, "Multiband asymmetric transmission of airborne sound by coded metasurfaces," *Phys. Rev. A, Gen. Phys.*, vol. 7, no. 2, Feb. 2017, Art. no. 024010.

[13] S. Liu, T. J. Cui, L. Zhang, Q. Xu, Q. Wang, X. Wan, J. Q. Gu, W. X. Tang, M. Qing Qi, J. G. Han, W. L. Zhang, X. Y. Zhou, and Q. Cheng, "Convolution operations on coding metasurface to reach flexible and continuous controls of terahertz beams," *Adv. Sci.*, vol. 3, no. 10, Oct. 2016, Art. no. 1600156.

[14] S. Liu and T. Jun Cui, "Flexible controls of terahertz waves using coding and programmable metasurfaces," *IEEE J. Sel. Topics Quantum Electron.*, vol. 23, no. 4, pp. 1–12, Aug. 2017.

[15] S. Liu and T. J. Cui, "Flexible controls of scattering clouds using coding metasurfaces," *Sci. Rep.*, vol. 6, no. 1, Dec. 2016.

[16] T.-J. Cui, S. Liu, and L.-L. Li, "Information entropy of coding metasurface," *Light, Sci. Appl.*, vol. 5, no. 11, p. e16172, Nov. 2016.

[17] S. Liu, T. J. Cui, Q. Xu, D. Bao, L. Du, X. Wan, W. X. Tang, C. Ouyang, X. Y. Zhou, H. Yuan, H. F. Ma, W. X. Jiang, J. Han, W. Zhang, and Q. Cheng, "Anisotropic coding metamaterials and their powerful manipulation of differently polarized terahertz waves," *Light, Sci. Appl.*, vol. 5, no. 5, p. e16076, May 2016.

[18] S. Liu, L. Zhang, Q. L. Yang, Q. Xu, Y. Yang, A. Noor, Q. Zhang, S. Iqbal, X. Wan, Z. Tian, W. X. Tang, Q. Cheng, J. G. Han, W. L. Zhang, and T. J. Cui, "Frequency-dependent dual-functional coding metasurfaces at terahertz frequencies," *Adv. Opt. Mater.*, vol. 4, no. 12, pp. 1965–1973, Dec. 2016.

[19] G. D. Bai, Q. Ma, S. Iqbal, L. Bao, H. B. Jing, L. Zhang, H. T. Wu, R. Y. Wu, H. C. Zhang, C. Yang, and T. J. Cui, "Multitasking shared aperture enabled with multiband digital coding metasurface," *Adv. Opt. Mater.*, vol. 6, no. 21, Nov. 2018, Art. no. 1800657.

[20] M. W. Beijersbergen, L. Allen, H. E. L. O. Van der Veen, and J. P. Woerdman, "Astigmatic laser mode converters and transfer of orbital angular-momentum," *Opt. Commun.*, vol. 96, pp. 123–132, Feb. 1993.

[21] S. Mohaghegh Mohammadi, L. K. S. Daldorff, J. E. S. Bergman, R. L. Karlsson, B. Thide, K. Forozesh, T. D. Carozzi, and B. Isham, "Orbital angular momentum in radio—A system study," *IEEE Trans. Antennas Propag.*, vol. 58, no. 2, pp. 565–572, Feb. 2010.

[22] P. Genevet, N. Yu, F. Aieta, J. Lin, M. A. Kats, R. Blanchard, M. O. Scully, Z. Gaburro, and F. Capasso, "Ultra-thin plasmonic optical vortex plate based on phase discontinuities," *Appl. Phys. Lett.*, vol. 100, no. 1, Jan. 2012, Art. no. 013101.

[23] F. Bouchard, I. D. Leon, S. A. Schulz, J. Upham, E. Karimi, and R. W. Boyd, "Optical spin-to-orbital angular momentum conversion in ultra-thin metasurfaces with arbitrary topological charges," *Appl. Phys. Lett.*, vol. 105, no. 10, 2014, Art. no. 101905.

[24] W. Wang, Y. Li, Z. Guo, R. Li, J. Zhang, A. Zhang, and S. Qu, "Ultra-thin optical vortex phase plate based on the metasurface and the angular momentum transformation," *J. Opt.*, vol. 17, no. 4, Apr. 2015, Art. no. 045102.

[25] M. W. Beijersbergen, R. P. C. Coerwinkel, M. Kristensen, and J. P. Woerdman, "Helical-wavefront laser beams produced with a spiral phaseplate," *Opt. Commun.*, vol. 112, pp. 321–327, Dec. 1994.

[26] L. Marrucci, C. Manzo, and D. Paparo, "Optical spin-to-orbital angular momentum conversion in inhomogeneous anisotropic media," *Phys. Rev. Lett.*, vol. 96, no. 16, Apr. 2006.

[27] J. Jin, J. Luo, X. Zhang, H. Gao, X. Li, M. Pu, P. Gao, Z. Zhao, and X. Luo, "Generation and detection of orbital angular momentum via metasurface," *Sci. Rep.*, vol. 6, no. 1, Apr. 2016, Art. no. 24286.

[28] Y. Tan, L. Li, and H. Ruan, "An efficient approach to generate microwave vector-vortex fields based on metasurface," *Microw. Opt. Technol. Lett.*, vol. 57, no. 7, pp. 1708–1713, Jul. 2015.

[29] R. Niemiec, C. Brousseau, K. Mahdjoubi, O. Emile, and A. Menard, "Characterization of an OAM flat-plate antenna in the millimeter frequency band," *IEEE Antennas Wireless Propag. Lett.*, vol. 13, pp. 1011–1014, 2014.

[30] P. Genevet, J. Lin, M. A. Kats, and F. Capasso, "Holographic detection of the orbital angular momentum of light with plasmonic photodiodes," *Nature Commun.*, vol. 3, no. 1, pp. 1–5, Jan. 2012.

[31] L. Zhang, R. Y. Wu, G. D. Bai, H. T. Wu, Q. Ma, X. Q. Chen, and T. J. Cui, "Transmission-reflection-integrated multifunctional coding metasurface for full-space controls of electromagnetic waves," *Adv. Funct. Mater.*, vol. 28, no. 33, Aug. 2018, Art. no. 1802205.

[32] D. Zhang, X. Cao, H. Yang, J. Gao, and X. Zhu, "Multiple OAM vortex beams generation using 1-bit metasurface," *Opt. Express*, vol. 26, no. 19, p. 24804, Sep. 2018.

[33] S. Liu, S. Liu, R. Y. Wu, G. D. Bai, Q. Ma, and T. J. Cui, "Polarization-selective dual-band digital coding metasurface for controls of transmitted waves," *J. Phys. D, Appl. Phys.*, vol. 51, no. 28, Jul. 2018, Art. no. 285103.

[34] R. F. Harrington, *Time-Harmonic Electromagnetic Fields*. New York, NY, USA: McGraw-Hill, 1961, pp. 460–463.

[35] M. R. Akram, M. Q. Mehmood, T. Tauqeer, A. S. Rana, I. D. Rukhlenko, and W. Zhu, "Highly efficient generation of bessel beams with polarization insensitive metasurfaces," *Opt. Express*, vol. 27, no. 7, pp. 9467–9480, Apr. 2019.

[36] M. R. Akram, M. Q. Mehmood, X. Bai, R. Jin, M. Premaratne, and W. Zhu, "High efficiency ultrathin transmissive metasurfaces," *Adv. Opt. Mater.*, vol. 7, no. 11, Jun. 2019, Art. no. 1801628.

[37] M. R. Akram, X. Bai, R. Jin, G. A. E. Vandenbosch, M. Premaratne, and W. Zhu, "Photon spin Hall effect-based ultra-thin transmissive metasurface for efficient generation of OAM waves," *IEEE Trans. Antennas Propag.*, vol. 67, no. 7, pp. 4650–4658, Jul. 2019.

[38] S. Tang, X. Li, W. Pan, J. Zhou, T. Jiang, and F. Ding, "High-efficiency broadband vortex beam generator based on transmissive metasurface," *Opt. Express*, vol. 27, no. 4, pp. 4281–4291, 2019.

[39] J. Wang, J.-Y. Yang, I. M. Fazal, N. Ahmed, Y. Yan, H. Huang, Y. Ren, Y. Yue, S. Dolinar, M. Tur, and A. E. Willner, "Terabit free-space data transmission employing orbital angular momentum multiplexing," *Nature Photon.*, vol. 6, no. 7, pp. 488–496, Jul. 2012.

[40] A. E. Willner, J. Wang, and H. Huang, "A different angle on light communications," *Science*, vol. 337, no. 6095, pp. 655–656, Aug. 2012.

[41] L. Yan, P. Gregg, E. Karimi, A. Rubano, L. Marrucci, R. Boyd, and S. Ramachandran, "Q-plate enabled spectrally diverse orbital-angular-momentum conversion for stimulated emission depletion microscopy," *Optica*, vol. 2, no. 10, p. 900, Oct. 2015.

[42] L. Zhou, W. Wen, C. T. Chan, and P. Sheng, "Electromagnetic-wave tunneling through negative-permittivity media with high magnetic fields," *Phys. Rev. Lett.*, vol. 94, no. 24, p. 2005, Jun. 2005.

[43] I. R. Hooper, T. W. Preist, and J. R. Sambles, "Making tunnel barriers (including metals) transparent," *Phys. Rev. Lett.*, vol. 97, no. 5, Aug. 2006, Art. no. 053902.

[44] K. Chen, G. Ding, G. Hu, Z. Jin, J. Zhao, Y. Feng, T. Jiang, A. Alú, and C. Qiu, "Directional janus metasurface," *Adv. Mater.*, vol. 32, no. 2, Jan. 2020, Art. no. 1906352.

[45] F. Yang, R. Deng, S. Xu, and M. Li, "Design and experiment of a near-zero-thickness high-gain transmit-reflect-array antenna using anisotropic metasurface," *IEEE Trans. Antennas Propag.*, vol. 66, no. 6, pp. 2853–2861, Jun. 2018.

[46] C. Menzel, C. Rockstuhl, and F. Lederer, "Advanced jones calculus for the classification of periodic metamaterials," *Phys. Rev. A, Gen. Phys.*, vol. 82, no. 5, Nov. 2010, Art. no. 053811.

[47] S. Iqbal, S. Liu, J. Luo, L. Zhang, H. A. Madni, and T. J. Cui, "Controls of transmitted electromagnetic waves for diverse functionalities using polarization-selective dual-band 2 bit coding metasurface," *J. Opt.*, vol. 22, no. 1, Jan. 2020, Art. no. 015104.

[48] S. Tang, T. Cai, G.-M. Wang, J.-G. Liang, X. Li, and J. Yu, "High-efficiency dual-modes vortex beam generator with polarization-dependent transmission and reflection properties," *Sci. Rep.*, vol. 8, no. 1, Dec. 2018, Art. no. 6422.

[49] W. Luo, S. Sun, H.-X. Xu, Q. He, and L. Zhou, "Transmissive ultrathin pancharatnam-berry metasurfaces with nearly 100% efficiency," *Phys. Rev. A, Gen. Phys.*, vol. 7, no. 4, Apr. 2017, Art. no. 044033.

[50] M. R. Akram, C. He, and W. Zhu, "Bi-layer metasurface based on Huygens' principle for high gain antenna applications," *Opt. Express*, vol. 28, no. 11, pp. 15844–15854, 2020.

SHAHID IQBAL received the M.Sc. and M.Phil. degrees in electronics from the Department of Electronics, Quaid-i-Azam University, Islamabad, Pakistan, in 2012 and 2015, respectively. He is currently pursuing the Ph.D. degree with the School of Information Science and Engineering, Southeast University, Nanjing, China. He is also a Researcher with the State Key Laboratory of Millimeter Waves, Southeast University. His research interests include metamaterials, metasurfaces with multi-functional features, plasmonics, antennas, and wave's propagation.

MUHAMMAD RIZWAN AKRAM (Graduate Student Member, IEEE) received the B.E. degree in electronic engineering from the Ghulam Ishaq Khan Institute of Engineering Sciences and Technology, Topi, Pakistan, in 2013, and the M.S. degree in information and communication engineering. He is currently pursuing the Ph.D. degree in electronic science and technology with Shanghai Jiao Tong University (SJTU), Shanghai, China. From January 2017 to June 2017, he was a Research Associate with Information Technology University, Lahore, Pakistan. He was a recipient of the IPC-Bilateral Scholarship to pursue his master's degree, in 2014, and the CSC Scholarship to pursue his Ph.D. degree, in 2017.

MUHAMMAD FURQAN (Graduate Student Member, IEEE) received the M.S. degree in multimedia and telecommunication from Muhammad Ali Jinnah University, Islamabad, Pakistan, in 2014. He is currently pursuing the Ph.D. degree with the Department of Information Science and Engineering, Southeast University, Nanjing, China. His research interests include opportunistic networks, mobile ad hoc networks, vehicular ad hoc networks, information centric networks, and optimization of future Internet.

HAMZA AHMAD MADNI received the B.S. degree in computer system engineering from NFCIET (BZU), Multan, Pakistan, in 2010, the M.S. degree in electrical and electronic engineering from the University of Bradford, U.K., in 2012, and the Ph.D. degree in electromagnetic field and microwave technology from Zhejiang University, China, in June 2017. He became an Assistant Professor with the Khwaja Fareed University of Engineering and Information Technology, Rahim Yar Khan, Pakistan. In December 2017, he was nominated for a Postdoctoral position at Southeast University (SEU), Nanjing, China, and completed in September 2019. His current research interests include transformation optics, coding metamaterials, antennas, invisibility cloaking, theoretical and numerical methods of electromagnetics, sensors, and controllers.

MUHAMMAD ISMAIL KHAN received the bachelor's degree in computer systems engineering from the University of Engineering and Technology, Peshawar, in 2007, the M.S. degree in electronic engineering from the Capital University of Sciences and Technology, Islamabad, Pakistan, and the Ph.D. degree from the National University of Sciences and Technology, Pakistan. During Ph.D. degree, his research was focused on design and analysis of metasurfaces for polarization control of GHz waves. He is currently working as an Assistant Professor with COMSATS University Islamabad, Pakistan. He is also working as a Postdoctoral Researcher with the School of Optics and Photonics, Beijing Institute of Technology, Beijing. His research interests include metasurfaces, metamaterials, antennas, quantum field theory, differential geometry, and complex manifolds.

GUOXIANG SHU received the Ph.D. degree from the University of Electronic Science and Technology of China, Chengdu, China, in 2017. He was a Visiting Researcher with the University of Strathclyde, U.K. Since September 2017, he has been an Assistant Professor with the College of Electronics and Information Engineering, Shenzhen University, China. He has authored/coauthored over 50 technical publications. His research interests include sheet electron beam TWTs, BWOs and EIOs, pseudospark-sourced electron beam devices, millimeterwave dielectric measurement, and passive devices (couplers, mode convertors, and resonant cavities). He has been recognized as the Shenzhen Overseas High-level Talents.

• • •